atoms

MDPI

Article

Influence of End Cap Structure on the Axial Geometric Parameter of the Linear Paul Trap

Lin Li [1,*] and Zi Li [2,3]

[1] School of Physics Electronics and Intelligent Manufacturing, Huaihua University, Huaihua 418000, China
[2] Innovation Academy for Precision Measurement Science and Technology, Chinese Academy of Sciences, Wuhan 430071, China; lizi@wipm.ac.cn
[3] University of Chinese Academy of Sciences, Beijing 100049, China
* Correspondence: lilin@hhtc.edu.cn

Abstract

Through finite-element simulation, the axial potential distribution of the ion trap is analyzed. The effects of the central hole diameter of the end cap and the spacing between the two end caps on the axial geometric parameters of the ion trap are investigated. Based on these findings, a set of linear Paul traps is designed by selecting suitable end caps and quadrupoles. Stable trapping of calcium ions (Ca^+) is successfully achieved, and these ions are subsequently laser-cooled into ionic Coulomb crystals. In the experiment, secular motion excitation of the Ca^+ ion Coulomb crystal is performed, yielding an axial geometric parameter of 0.115(1) for the ion trap. This value aligns well with the simulation result of 0.114(2). The precise determination of the axial geometric parameter provides a solid foundation for subsequent high-precision optical or mass spectrometry measurements.

Keywords: linear Paul trap; axial geometric parameter; end cap; secular motion excitation

1. Introduction

Trapped atomic ions are widely used in experiments and applications. The development of high-accuracy ion clocks [1] and their role in tests of fundamental physics using trapped ions [2] underscore the importance of precise control and measurement of ion dynamics. These advancements have been crucial in demonstrating the significance of trapped ions in quantum computing [3,4], where long coherence times and high-fidelity operations are critical. Additionally, ionic Coulomb crystals have facilitated the sympathetic cooling of molecular ions [5,6], thereby expanding the scope of trapped ion applications. These developments are further supported by continuous improvements in ion trap design [7], which enhance experimental precision and stability.

When the trapped ions are laser-cooled down to a few millikelvin, an ordered structure is formed, called the ionic Coulomb crystal [8]. Ionic Coulomb crystals can be used to sympathetically cool molecular ions or highly charged ions that are difficult to laser-cooled [9,10]. Currently, ions can be trapped primarily in Penning traps or Paul traps, which represent the two most widely used electromagnetic configurations for precision spectroscopy and quantum computing. In a Penning trap, the ions are trapped by an electrostatic field combined with a static magnetic field [11]. In a Paul trap, the ions are trapped by an electrostatic field and a varying time-dependent electric field, typically in the radio-frequency (rf) domain [12]. The most commonly used is the linear Paul trap. A typical linear Paul trap consists of a quadrupole for radial confinement of the ions and two end caps for axial confinement of the ions [13].

Check for updates

Academic Editor: Pascal Quinet

Received: 19 November 2025
Revised: 3 February 2026
Accepted: 3 February 2026
Published: 5 February 2026

Copyright: © 2026 by the authors. Licensee MDPI, Basel, Switzerland. This article is an open access article distributed under the terms and conditions of the Creative Commons Attribution (CC BY) license.

Due to the cylindrical electrode being easier to process than the hyperbolic electrode, a cylindrical quadrupole is usually used instead of the hyperbolic quadrupole. To reduce the effect of the dodecapole electric potential, the ratio of the electrode radius to the minimum spacing from the trap center to the electrode surface is close to 1.14511 [14]. There are generally several designs for the end cap, such as placing two thin cylinders between the quadrupoles [13,15,16], a lens electrode pair placed at the end of a quadrupole rod [17,18] or the commonly used segmented linear Paul trap [19,20]. The design of thin cylindrical or lens electrode requires additional mechanical support. Thin cylindrical electrodes are simpler to design and fabricate, yet their placement on the quadrupole axis will block axial ion injection and optical access. Lens electrode has a certain focusing effect on the ions. A sufficiently large static voltage is necessary to ensure tight confinement at the trap center, rather than merely preventing ion escape at the axial ends. This becomes essential when end caps are positioned farther from the center to counteract quadrupole shielding, thereby enhancing laser cooling efficiency and improving laser spectroscopy. So it needs to find a configuration, which can help to counteract the reduced electric field strength due to the shielding effect of the quadrupoles, thereby ensuring stable trapping of ions over a larger axial range. The segmented ion traps can precisely control the position of the ion Coulomb crystal, but the structure is more complex, and the processing of the segmented ion trap requires high precision.

The approximation of the potential near the center of the ion trap as an ideal electric quadrupole potential, which is based on the assumption that higher-order terms in the potential expansion are negligible within the central region of the trap. This assumption is valid when the ions are confined close to the trap center, where the quadrupole term dominates the potential distribution. The motion of the ions in the center of the trap is simple harmonic motion because the quadratic potential approximation is valid for small displacements. Then the motion is divided into axial secular motion and radial secular motion, and the frequencies of both axial and radial secular motion are correlated with the mass-to-charge ratios of the ions [7]. The axial and radial secular motions are decoupled in this regime, allowing for the analysis of their frequencies independently. Then the mass-to-charge ratios of the trapped ions can be determined by measuring the secular motion frequency of the trapped ions, e.g., by using the axial secular motion excitation or the radial secular motion excitation [19,21–23]. Different end cap geometries and end cap spacing affect the axial potential distribution, which in turn affects the magnitude of the axial and radial secular motion frequencies of the ions. To obtain accurate mass spectra, it is necessary to precisely obtain the influence of the end cap geometry, referred to as the axial geometric parameter [24]. The axial geometric parameter is a critical parameter in ion traps, directly linking the measured secular frequencies of trapped ions to their mass-to-charge ratios. This precise determination of the axial geometric parameter provides a solid foundation for subsequent high-precision optical spectroscopy measurements, enabling applications such as tests of quantum electrodynamics (QED) and precise determination of fundamental constants [5–7].

In this paper, we have designed a square end cap with a central hole for the purpose of enabling axial ion injection and axial laser passage. This end cap is mounted on a cylindrical quadrupole and can be adjusted in spacing by sliding. Through simulating and analyzing the axial potential of the ion trap, we have investigated the influence of the diameter of the central circular hole in the end cap as well as the spacing between the two end caps on the axial geometric parameter of the ion trap. To obtain the axial geometric parameter of the ion trap, we employ two methods: experimentally, by utilizing axial secular motion excitation of the Coulomb crystal of Ca^+ ions; and analytically, by examining the axial potential field distribution through finite-element simulations.

2. Experiment

The linear Paul trap used in the experiment is shown in Figure 1a and is placed in a stainless steel chamber with a background pressure below 1×10^{-10} mbar [25]. The quadrupole of the ion trap consists of four stainless steel hollow cylindrical rods with a length of 80 mm, an outer diameter of 8 mm, and an inner diameter of 6 mm. Four ceramic rods, 100 mm long and 6 mm in diameter, are passed through the quadrupole rods, ensuring a snug fit for mechanical support and electrical insulation. To minimize charging effects on the ceramic rods, we used high-purity alumina rods and applied a thin insulating coating. Periodic checks on the trap performance have shown no significant perturbations due to charging effects.

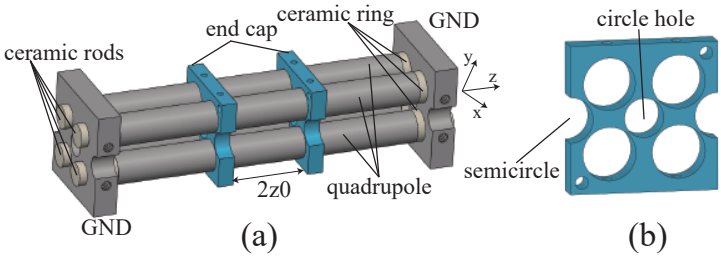

Figure 1. (color online) The linear Paul trap used in the experiment includes: (**a**) A 3D diagram showing the quadrupole rods, ceramic insulators, end caps, and GND terminals, with $2z_0$ indicating the spacing between two end caps. (**b**) An isometric view of the end cap with a central hole for ion injection/ejection.

The blue electrode serves as the ion trap's end cap. As illustrated in the three-dimensional schematic in Figure 1b, it features a cross-section of a square with a 22.6 mm side length and a width of 4 mm. The semicircle cutouts on the end cap of the ion trap, each with a diameter of 6 mm, are precisely engineered to provide a radial optical access region. Additionally, a central hole in the center of the end cap to facilitate the axial injection of ions and axial laser passage. 4 holes of 8.2 mm diameter are arranged in a square with a spacing of 10.6 mm between adjacent holes, and a quadrupole passes through the hole, which is insulated by a polyimide tape between the quadrupole and the end cap. The spacing between the end caps can be regulated by sliding them accordingly. The two stainless-steel square holders with a 27 mm square bottom, a width of 4 mm, and a 6 mm hole in the center, are grounded (GND) and fix the ceramic rods. Square holders and quadrupoles are insulated by a 2 mm-thick ceramic ring with outer diameter of 8 mm and inner diameter of 6 mm. Further details on the mechanical assembly and insulation procedures are provided in our previous work [26].

Radial confinement of the ions is achieved by applying an rf voltage with a frequency of $\Omega_{\mathrm{rf}} = 2$ MHz and a peak-to-peak voltage of V_{rf} ranging from 100 V to 300 V to the quadrupole, the radial secular frequency varies from $2\pi \times 175$ kHz to $2\pi \times 525$ kHz. Axial confinement of the ions is performed by applying a static voltage U_{end} on the end cap, and the static voltage on the end cap produces the following potential distribution in the axial direction of the ion trap [7]:

$$\phi(z) = \frac{\kappa_z Q U_{\mathrm{end}} z^2}{z_0^2}, \tag{1}$$

where κ_z is the ion trap axial geometric parameter, Q is the charge of the ion, z is the axial coordinate with origin at trap center, and $2z_0$ is the spacing between the inner surfaces of the two end cap electrodes.

The potential distribution at locations near the center of the ion trap can be viewed as a harmonic potential with the following expression:

$$\phi(z) = \frac{1}{2} M \omega_z^2 z^2, \tag{2}$$

where M denotes the mass of the ion and ω_z denotes the frequency of the axial secular motion of the ion with the following expression:

$$\omega_z^2 = \frac{2\kappa_z Q U_{\text{end}}}{M z_0^2}, \tag{3}$$

From the above equations, the axial geometric parameter κ_z can be obtained by two methods: 1. the axial potential distribution of the ion trap is obtained by finite-element numerical calculations, and then it can be obtained by fitting from Equation (1); 2. the axial secular motion frequency of the trapped ion Coulomb crystal is obtained by axial secular motion excitations under different end cap voltage [24,27], and then it can be obtained by fitting from Equation (3). The axial-to-radial frequency ratio ω_z/ω_r is kept below 0.6, which can keep crystal stability and mass resolution [7].

Finite-element numerical calculations are performed using COMSOL Multiphysics 6.4 (AC/DC Module). For the basic configuration, a stationary study is chosen because only the static electric-potential distribution is required, both the output and the values of dependent-variable are physics controlled. The Electrostatics interface models the trap geometry with an adaptive tetrahedral mesh: a minimum element size of 0.022 mm is imposed near the trap centre to resolve steep field gradients, while a maximum element size of 2.2 mm is retained in outer regions. Mesh independence is confirmed by varying the resolution and monitoring the potential stability at the trap center (<1% change). The resulting linear system is solved iteratively with the conjugate-gradient method, and convergence is accepted when the relative residual tolerance reaches 0.01.

In the experiment, Ca^+ ions are generated via laser ablation of a 99%-pure, 0.4-mm-thick calcium target, which is aligned axially 55 mm away from the entrance end cap [25]. A diode-pumped pulsed laser, operating at a wavelength of 1064 nm with a pulse width of 8 ns and energy of 10–200 μJ/pulse, is focused on the target to induce ablation. The ablated Ca^+ ions then pass through the entrance end cap and are guided by the quadrupole to the center of the trap. To load Ca^+ ions into the ion trap, the voltage of the entrance end cap is modulated (switched on and off). Subsequently,the ions are collisionally cooled down to several hundred K using helium gas (99.9999% purity, room temperature ∼300 K). The buffer gas is introduced into the vacuum chamber through a manual leak valve (Kurt Lesker, VZLVM267, Jefferson Hills, PA, USA), opened manually to maintain a background pressure of about 10^{-6} mbar for 2–3 s. The gas is then pumped away by the turbomolecular pump, allowing the pressure to decay back to the base value of 10^{-10} mbar with approximately 30 s, ensuring a clean and stable environment for ion trapping.

After buffer gas collisional cooling, the ions are then laser-cooled to the mK regime to an ordered ionic Coulomb crystal. The laser cooling process involves two primary lasers: a 397 nm laser for cooling and an 866 nm laser for repumping. The 397 nm laser is red-detuned by 20 MHz from the resonant frequency of the dipole transition $4s\,^2S_{1/2} \leftrightarrow 4p\,^2P_{1/2}$, while the 866 nm laser is resonant on the transition $4p\,^2P_{1/2} \leftrightarrow 3d\,^2D_{3/2}$. The stable isotope $^{40}Ca^+$ is used in our experiments. Both the 397 nm and 866 nm lasers are operated at 1 mW with 1 mm spot sizes. The image of the ion Coulomb crystal is detected by a CCD camera (Andor iKon-M 934, Belfast, UK), and the fluorescence emitted by the ions is counted by a photomultiplier (Thorlabs PMT1002, Newton, NJ, USA). The imaging optics used with the CCD camera include a high-quality lens

with a numerical aperture of 0.18 and a magnification of 6x, providing a resolution of approximately 2.2 μm. The CCD integration time is set to 2 seconds to balance the signal strength and reduce noise.

3. Results and Discussion

When the spacing between the two end caps is 20 mm and the diameter of the circular hole at the center of the end cap is 6 mm, the region within 2 mm from the trap center is selected for simulation and analysis of the axial potential distribution. The potential of the two end caps is set to 10 V. Then the final axial potential distribution of the ion trap is shown in Figure 2. Fitting Equation (1) yields a value of $\kappa_z = 0.1299$. Subsequent simulations vary the diameters of the circular holes to determine the corresponding axial geometric parameters for different circular hole diameters.

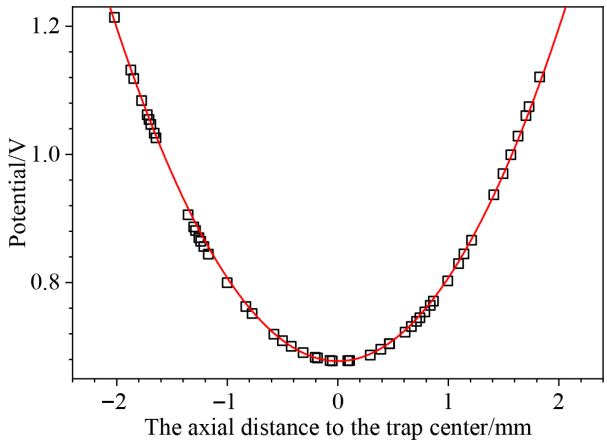

Figure 2. (color online) The axial potential from ±2 mm to the center of the trap, the black hollow square scatter plot is the simulated values and the red parabola solid line is a fitting of the simulated values.

The diameter of the circular hole can be chosen between 0 and 16 mm, given that the square end cap has a side length of 22.6 mm. To investigate how the axial geometric parameter changes when the circular hole's diameter exceeds 16 mm, simulations are conducted using round end caps. These end caps are 30-mm-diameter, 4-mm-thick cylindrical electrodes with a single on-axis hole; no lateral cut-outs are machined. Here, the spacing between the two end caps is fixed at 20 mm. As shown in Figure 3, the axial geometric parameter varies with the diameter of the center circular hole for both square and round end caps. It is observed that the axial geometric parameter is approximately the same for round and square end caps when the circular hole has the same diameter. For both square and round end caps, the axial geometric parameter decreases as the diameter of the circular hole increases. When the diameter of the circular hole is in the range of 0 to 4 mm, the axial geometric parameter remains approximately 0.16. As the diameter increases from 4 mm to 14 mm, the axial geometric parameter decreases rapidly from 0.16 to 0.003. When the diameter exceeds 14 mm, the axial geometric parameter stabilizes near 0.001.

Setting the end-cap hole to 6 mm lets the cooling light pass unclipped, keeps ion injection efficient, and preserves enough axial curvature for a usable trap depth, all with a drill-bit-friendly diameter. Additionally, the effect of the spacing between the two end caps on the ion trap's axial geometric parameter is examined. The spacing between the two end caps is varied within a range of 2–27 mm, and the corresponding variation of the axial geometric parameter with this distance is shown in Figure 4. When the spacing between the two end caps is in the range of 1–9 mm, the axial geometric parameter increases with increasing spacing between the two end caps. As the end caps

are brought closer together, the quadrupole rods shield a larger portion of the end cap field, reducing its effective strength and thus the axial geometric parameter increase. When the spacing between the two end caps is greater than 9 mm, the axial geometric parameter begins to decrease with further increases in spacing between the two end caps, which is due to the increased shielding effect of the quadrupole rods on the end cap electric field. The axial geometric parameter reaches its maximum value when the spacing between the two end caps is 9 mm.

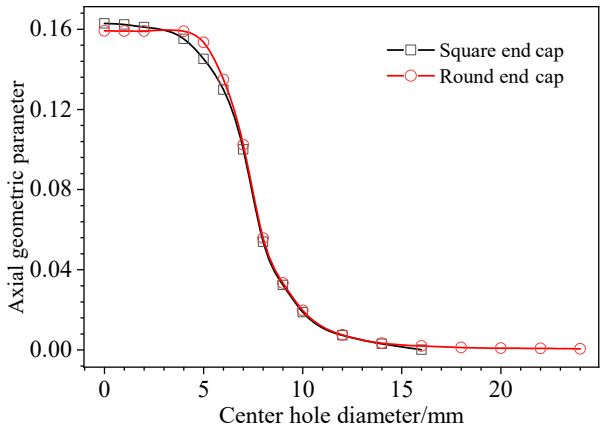

Figure 3. (color online) The influence of end cap shape and center hole diameter on the axial geometric parameter, the solid line is a cubic spline interpolation guide to the eye. Simulated uncertainties are smaller than marker size.

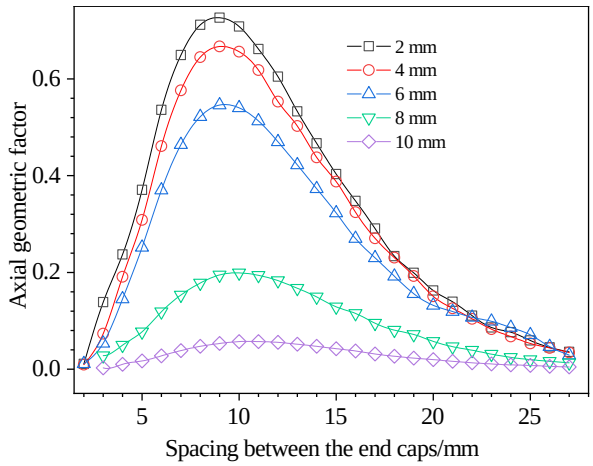

Figure 4. (color online) The simulated axial geometric parameter of the square end cap with diameters of 2, 4, 6, 8, 10 mm center hole at different spacings. The solid line is a cubic spline interpolation guide to the eye.

Subsequently, to ascertain whether the optimum end-cap separation is sensitive to the central-bore diameter, the axial geometric parameter is mapped as a function of end-cap spacing for the diameter of the center hole as 2, 4, 6, 8 and 10 mm. The resulting curves (Figure 4) exhibit a systematic shift of the peak position: end-cap spacing about 9 mm for the diameter of the center hole as 2, 4, 6 mm, whereas it migrates to about 10 mm for the diameter of the center hole as 8 mm and 10 mm. Irrespective of this 1 mm displacement, the asymmetric peaked functional form of the axial geometric parameter remains essentially unchanged, indicating that the qualitative tuning characteristics of the trap are preserved across the entire aperture range investigated.

Within the experimental setup, the end cap voltage is adjustable between 0 and 200 V. Considering that the average velocity of sputtered ions is typically about 10 mm/μs [28,29],

calcium ions possess a corresponding mean kinetic energy of ≈20.8 eV. To load the majority of these ions, the axial potential-well depth of the trap must therefore be comparable to this average kinetic energy. To load high kinetic energy ions generated by laser ablation, a maximum axial potential trap depth of 20 eV is required. This corresponds to an axial geometric parameter of approximately 0.1. A spacing of about 4 mm or 21 mm between the two end caps is needed. Since a larger spacing between the end caps results in a larger trapping area and the ability to trap more ions, a spacing of approximately 21 mm is chosen. The actual spacing during assembly is 20.70(5) mm with 16 measurements distributed evenly between the two end caps' inner surface, the uncertainty primarily arises from the precision limit of the vernier caliper. The diameter of the center hole at the end cap is set to 6 mm, with a machining uncertainty of 0.01 mm. Through simulation analysis, the axial geometric parameter of the ion trap after assembly is determined to be 0.114(2).

The ion Coulomb crystal is formed through trapping and laser cooling using the designed ion trap. The images shown in Figure 5 of the ion Coulomb crystals are obtained using a CCD to capture the fluorescence emitted by the trapped ions. The ion Coulomb crystals are formed by trapping and laser cooling the ions in the designed ion trap. The fluorescence intensity is recorded under different end cap voltages, resulting in different shapes of the ion Coulomb crystals. The quadrupole is driven at $V_{\mathrm{rf,p-p}} = 100$ V, corresponding to a radial secular frequency of $2\pi\times175$ kHz, while the end-cap voltage is varied to shape the ion Coulomb crystal from prolate ellipsoid to oblate ellipsoid, as shown in Figure 5. No significant dark ions from minor isotopes are observed, likely due to their low abundance and the absence of laser cooling, which may have led to their ejection from the trap. The number density of the ion Coulomb crystal is calculated under the zero-temperature approximation [30]. By approximating the ion Coulomb crystal as an ellipsoid and fitting an ellipse to the contour of the ion fluorescence image, the volume of the crystal is determined. The ion Coulomb crystal shown in Figure 5 contains approximately 4000 ions.

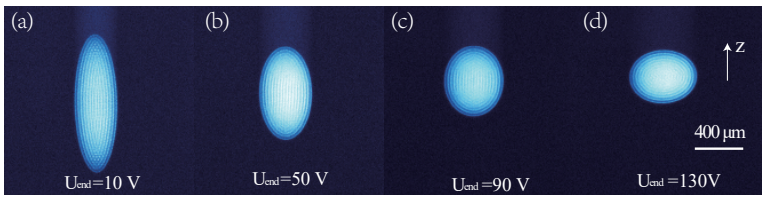

Figure 5. (color online) Fluorescence images of ion Coulomb crystals captured using a CCD camera. The crystals are formed by trapping and laser-cooling ions in the designed ion trap under different end cap voltages: (**a**) 10 V, (**b**) 50 V, (**c**) 90 V, and (**d**) 130 V. Variations in the end cap voltage produce different axial confinement strengths, resulting in the observed diversity of crystal shapes.

To verify the reliability of the simulation analysis, the axial geometric parameter of the ion trap is determined experimentally by secular-motion excitation. An rf voltage with an amplitude of 40 mV is applied to one end cap to perform secular motion excitation on the Ca^+ ion Coulomb crystal, as shown in Figure 6. The rf frequency is scanned from 70 kHz to 100 kHz. When the applied rf frequency matches the secular motion frequency of the ion Coulomb crystal, the crystal is heated, leading to a change in fluorescence intensity. The increase in fluorescence intensity at resonance is due to the enhanced excitation of the ions, leading to more efficient fluorescence emission. Although the ions gain kinetic energy and the crystal structure is perturbed, the ions remain trapped within the potential well. The fluorescence maximum marks the point of most efficient photon production. Here, the 397 nm laser is red-detuned by 20 MHz. This detuning, larger than the usual 10 MHz, is chosen to produce an upward fluorescence peak that contrasts clearly with the off-resonance background. At an end-cap bias of 30 V (Figure 6), the fluorescence peak

emerges when the rf drive frequency coincides with the axial secular frequency of the Coulomb crystal, revealing the resonant amplification of the ions' collective secular motion.

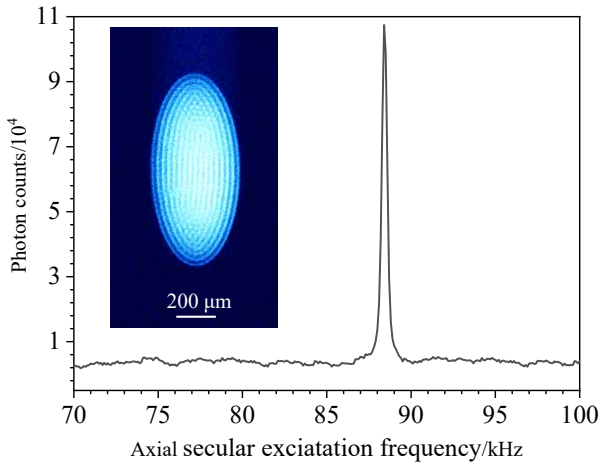

Figure 6. (color online) The inset shows the crystal without motional excitation at U_{end} = 30 V. Secular motion excitation is performed and the fluorescence of ions changes with the secular motion excitation rf frequency, the resonance curve is not background-subtracted.

We performed axial-secular-excitation measurements on five Coulomb-crystal sizes: N ≈ 50, 100, 500, 2000 and 10,000 ions. For each N we recorded the secular frequency ω_z at end-cap voltages, linear fitted ω_z^2 vs U_{end} with Equation (3) yields an uncertainty of about 2%, and extracted κ_z. Figure 7 shows the data for N = 100 and 10,000 as representative examples. The rf voltage is maintained at 100 V while the end cap voltage is varied from 10 V to 80 V. For an end cap spacing of $2z_0$=20.70(5) mm, the resulting κ_z values for the five sizes are 0.116(3), 0.115(2), 0.114(2), 0.114(3) and 0.115(3), respectively, exhibiting no systematic dependence on crystal size. A weighted average of these five independent determinations yields the final experimental κ_z = 0.115(1), which shows a high degree of consistency with the simulation results.

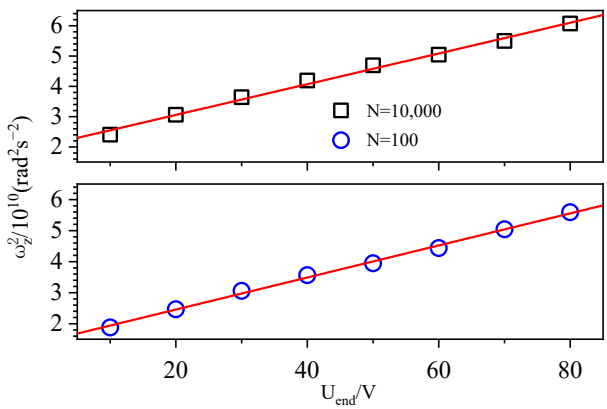

Figure 7. (color online) For Ca^+ ion Coulomb crystals of different sizes, the square of the secular motion frequency changes with the end cap voltages.

4. Conclusions

This study utilizes finite-element simulations to explore the impact of the central circular hole's diameter in the end cap and the spacing between the two end caps on the ion trap's axial geometric parameter. Based on these insights, a linear Paul trap is designed by selecting the central hole diameter and end cap spacing. The successful trapping of Ca^+ ions and the formation of ion Coulomb crystals are achieved. By examining crystals of different sizes and performing secular motion excitation at various end cap voltages, the ion

trap's axial geometric parameter is measured as 0.115(1). This experimental value closely matches the simulation-derived parameter of 0.114(2). In contrast, the axial geometric parameters vary across different configurations, such as our previous trap with a parameter of 0.374(2) [24], and other linear Paul traps with parameters of 0.244 and 0.342 [31,32], respectively. This reduction originates from the present end-cap design: the 6 mm central hole maintains axial laser access and focusing of injected ions, while the 20.7 mm end-cap separation (almost four times that of refs. [24,32]) expands the trapping region, increasing the typical loaded ion number from a few hundred to several thousand. Thus, the smaller axial geometric parameter is a direct consequence of optimizing the trap for axial injection and large Coulomb crystals rather than for maximal electric field curvature.

Upon determining the precise axial geometric parameter, one can calculate both the axial and radial secular motion frequencies for ions with varying mass-to-charge ratios. This enables the identification of different ion species within trapped multicomponent ion Coulomb crystals through secular motion excitation [33,34]. Alternatively, by employing axial secular motion excitation, ions resonating with the excitation frequency can be extracted axially, facilitating the acquisition of high-precision mass spectra [35,36].

Author Contributions: Writing—original draft preparation, L.L. and Z.L.; writing—review and editing, L.L. and Z.L.; supervision, L.L. All authors have read and agreed to the published version of the manuscript.

Funding: This research received no external funding.

Data Availability Statement: All data that support the findings of this study are included within the article.

Conflicts of Interest: The authors declare no conflicts of interest.

References

1. Huang, Y.; Zhang, B.; Zeng, M.; Hao, Y.; Ma, Z.; Zhang, H.; Guan, H.; Chen, Z.; Wang, M.; Gao, K. Liquid-nitrogen-cooled Ca^+ optical clock with systematic uncertainty of 3×10^{-18}. *Phys. Rev. Appl.* **2022**, *17*, 034041. [CrossRef]
2. Brewer, S.M.; Chen, J.S.; Hankin, A.M.; Clements, E.R.; Chou, C.w.; Wineland, D.J.; Hume, D.B.; Leibrandt, D.R. $^{27}Al^+$ quantum-logic clock with a systematic uncertainty below 10^{-18}. *Phys. Rev. Lett.* **2019**, *123*, 033201. [CrossRef] [PubMed]
3. Lu, Y.; Zhang, S.; Zhang, K.; Chen, W.; Shen, Y.; Zhang, J.; Zhang, J.N.; Kim, K. Global entangling gates on arbitrary ion qubits. *Nature* **2019**, *572*, 363–367. [CrossRef] [PubMed]
4. Debnath, S.; Linke, N.M.; Figgatt, C.; Landsman, K.A.; Wright, K.; Monroe, C. Demonstration of a small programmable quantum computer with atomic qubits. *Nature* **2016**, *536*, 63–66. [CrossRef]
5. Alighanbari, S.; Giri, G.; Constantin, F.L.; Korobov, V.; Schiller, S. Precise test of quantum electrodynamics and determination of fundamental constants with HD^+ ions. *Nature* **2020**, *581*, 152–158. [CrossRef]
6. Kortunov, I.; Alighanbari, S.; Hansen, M.; Giri, G.; Korobov, V.; Schiller, S. Proton–electron mass ratio by high-resolution optical spectroscopy of ion ensembles in the resolved-carrier regime. *Nat. Phys.* **2021**, *17*, 569–573. [CrossRef]
7. Berkeland, D.; Miller, J.; Bergquist, J.C.; Itano, W.M.; Wineland, D.J. Minimization of ion micromotion in a Paul trap. *J. Appl. Phys.* **1998**, *83*, 5025–5033. [CrossRef]
8. Thompson, R.C. Ion coulomb crystals. *Contemp. Phys.* **2015**, *56*, 63–79. [CrossRef]
9. King, S.A.; Spieß, L.J.; Micke, P.; Wilzewski, A.; Leopold, T.; Benkler, E.; Lange, R.; Huntemann, N.; Surzhykov, A.; Yerokhin, V.A.; et al. An optical atomic clock based on a highly charged ion. *Nature* **2022**, *611*, 43–47. [CrossRef]
10. Koelemeij, J.; Roth, B.; Wicht, A.; Ernsting, I.; Schiller, S. Vibrational spectroscopy of HD^+ with 2-ppb accuracy. *Phys. Rev. Lett.* **2007**, *98*, 173002. [CrossRef]
11. Dehmelt, H.G. Radiofrequency spectroscopy of stored ions I: Storage. In *Advances in Atomic and Molecular Physics*; Elsevier: Amsterdam, The Netherlands, 1968; Volume 3, pp. 53–72.
12. Paul, W. Electromagnetic traps for charged and neutral particles. *Rev. Mod. Phys.* **1990**, *62*, 531. [CrossRef]
13. Prestage, J.; Dick, G.J.; Maleki, L. New ion trap for frequency standard applications. *J. Appl. Phys.* **1989**, *66*, 1013–1017. [CrossRef]
14. Reuben, A.; Smith, G.; Moses, P.; Vagov, A.; Woods, M.; Gordon, D.; Munn, R. Ion trajectories in exactly determined quadrupole fields. *Int. J. Mass Spectrom. Ion Processes* **1996**, *154*, 43–59. [CrossRef]

15. Hashimoto, Y.; Matsuoka, L.; Nagamoto, D.; Hasegawa, S. Observation of single Ca^+ ions for trace isotope analysis. *Spectrochim. Acta Part B At. Spectrosc.* **2008**, *63*, 645–651. [CrossRef]
16. Kitaoka, M.; Hasegawa, S. Isotope-selective manipulation of Ca^+ using laser heating and cooling in a linear Paul trap. *J. Phys. B At. Mol. Opt. Phys.* **2012**, *45*, 165008. [CrossRef]
17. Guna, M.; Biesenthal, T.A. Performance enhancements of mass selective axial ejection from a linear ion trap. *J. Am. Soc. Mass Spectrom.* **2011**, *20*, 1132–1140. [CrossRef]
18. Dobson, G.S.; Enke, C.G. Axial focusing following low kinetic energy pulsed extraction from a miniature linear ion trap. *Rapid Commun. Mass Spectrom.* **2007**, *21*, 2905–2912. [CrossRef]
19. Baba, T.B.T.; Waki, I.W.I. Cooling and mass-analysis of molecules using laser-cooled atoms. *Jpn. J. Appl. Phys.* **1996**, *35*, L1134. [CrossRef]
20. Drewsen, M.; Jensen, I.; Lindballe, J.; Nissen, N.; Martinussen, R.; Mortensen, A.; Staanum, P.; Voigt, D. Ion Coulomb crystals: A tool for studying ion processes. *Int. J. Mass Spectrom.* **2003**, *229*, 83–91. [CrossRef]
21. Roth, B.; Fröhlich, U.; Schiller, S. Sympathetic Cooling of $^4He^+$ Ions in a Radio-Frequency Trap. *Phys. Rev. Lett.* **2005**, *94*, 053001. [CrossRef] [PubMed]
22. Baba, T.; Waki, I. Laser-cooled fluorescence mass spectrometry using laser-cooled barium ions in a tandem linear ion trap. *J. Appl. Phys.* **2001**, *89*, 4592–4598. [CrossRef]
23. Kimura, N.; Okada, K.; Takayanagi, T.; Wada, M.; Ohtani, S.; Schuessler, H.A. Sympathetic crystallization of CaH^+ produced by a laser-induced reaction. *Phys. Rev. A* **2011**, *83*, 033422. [CrossRef]
24. Li, H.; Zhang, Y.; He, S.; Tong, X. Determination of the geometric parameters κ_z and κ_r of a linear Paul trap. *Chin. J. Phys.* **2019**, *60*, 61–67. [CrossRef]
25. Li, L.; Li, Z.; Hua, X.; Tong, X. Dynamic laser ablation loading of a linear Paul trap. *J. Phys. D Appl. Phys.* **2024**, *57*, 315205. [CrossRef]
26. Li, Z.; Gan, W.T.; Wang, C.; Li, L.; Hua, X.; Tong, X. Trapping and sympathetic cooling of Th^{3+} ions in a linear ion trap. *J. Appl. Phys.* **2025**, *138*, 224901. [CrossRef]
27. Li, H.X.; Li, M.; Zhang, Q.Y.; Tong, X. Secular Motion Frequencies of $^9Be^+$ Ions and $^{40}Ca^+$ Ions in Bi-component Coulomb crystals. *Chin. Phys. Lett.* **2019**, *36*, 073701. [CrossRef]
28. Thestrup, B.; Toftmann, B.; Schou, J.; Doggett, B.; Lunney, J. Ion dynamics in laser ablation plumes from selected metals at 355 nm. *Appl. Surf. Sci.* **2002**, *197*, 175–180. [CrossRef]
29. Campbell, C.J. Trapping, Laser Cooling, and Spectroscopy of Thorium IV. Ph.D. Thesis, Georgia Institute of Technology, Atlanta, GA, USA, 2011.
30. Hornekær, L.; Kjærgaard, N.; Thommesen, A.; Drewsen, M. Structural properties of two-component Coulomb crystals in linear Paul traps. *Phys. Rev. Lett.* **2001**, *86*, 1994. [CrossRef]
31. Zhong, Z.X.; Tong, X.; Yan, Z.C.; Shi, T.Y. High-precision spectroscopy of hydrogen molecular ions. *Chin. Phys. B* **2015**, *24*, 053102. [CrossRef]
32. Tong, X.; Winney, A.H.; Willitsch, S. Sympathetic Cooling of Molecular Ions in Selected Rotational and Vibrational States Produced by Threshold Photoionization. *Phys. Rev. Lett.* **2010**, *105*, 143001. [CrossRef] [PubMed]
33. Blythe, P.; Roth, B.; Fröhlich, U.; Wenz, H.; Schiller, S. Production of ultracold trapped molecular hydrogen ions. *Phys. Rev. Lett.* **2005**, *95*, 183002. [CrossRef] [PubMed]
34. Zhang, Y.; Zhang, Q.Y.; Bai, W.L.; Peng, W.C.; He, S.G.; Tong, X. An efficient preparation of HD^+ molecular ions in an ion trap by REMPI. *Chin. J. Phys.* **2023**, *84*, 164–172. [CrossRef]
35. Willitsch, S.; Bell, M.T.; Gingell, A.D.; Procter, S.R.; Softley, T.P. Cold reactive collisions between laser-cooled ions and velocity-selected neutral molecules. *Phys. Rev. Lett.* **2008**, *100*, 043203. [CrossRef] [PubMed]
36. Higaki, H.; Ito, K.; Takai, R.; Nakayama, K.; Saiki, W.; Izawa, K.; Okamoto, H. Axial resonances of Ar^+ ions observed in a linear Paul trap. In *TCP 2006: Proceedings of the 4th International Conference on Trapped Charged Particles and Fundamental Physics (TCP 2006), Parksville, Canada, 3–8 September 2006*; Springer: Berlin/Heidelberg, Germany, 2007; pp. 433–438.

Disclaimer/Publisher's Note: The statements, opinions and data contained in all publications are solely those of the individual author(s) and contributor(s) and not of MDPI and/or the editor(s). MDPI and/or the editor(s) disclaim responsibility for any injury to people or property resulting from any ideas, methods, instructions or products referred to in the content.